JOURNAL OF APPLIED PHYSICS **97**, 083507 (2005)

Noncontacting laser photocarrier radiometric depth profilometry of harmonically modulated band bending in the space-charge layer at doped SiO_2-Si interfaces

Andreas Mandelis[a)]
Institute für Experimentalphysik III, Festkörperspekroskopie, Ruhr-Universität Bochum, Bochum D-44801, Germany and Center for Advanced Diffusion-Wave Technologies, Department of Mechanical and Industrial Engineering, University of Toronto, Ontario, M5S 3G8, Canada

Jerias Batista
Center for Advanced Diffusion-Wave Technologies, Department of Mechanical and Industrial Engineering, University of Toronto, Ontario, M5S 3G8, Canada

Jürgen Gibkes
Institut für Experimentalphysik III, Festkörperspekroskopie, Ruhr-Universität Bochum, Bochum D-44801, Germany

Michael Pawlak
Institut für Experimentalphysik III, Festkörperspekroskopie, Ruhr-Universität Bochum, Bochum D-44801, Germany and Institute of Physics, Nicolaus Copernicus University, Grudziadzka 5/7, 87-100 Torun, Poland

Josef Pelzl
Institut für Experimentalphysik III, Festkörperspekroskopie, Ruhr-Universitat Bochum, Bochum D-44801, Germany

(Received 2 June 2004; accepted 29 November 2004; published online 1 April 2005)

Laser infrared photocarrier radiometry (PCR) was used with a harmonically modulated low-power laser pump and a superposed dc superband-gap optical bias (a secondary laser beam) to control and monitor the space-charge-layer (SCL) width in oxidized *p*-Si–SiO_2 and *n*-Si–SiO_2 interfaces (wafers) exhibiting charged interface-state related band bending. Applying the theory of PCR-SCL dynamics [A. Mandelis, J. Appl. Phys. **97**, 083508 (2005)] to the experiments yielded various transport parameters of the samples as well as depth profiles of the SCL exhibiting complete (*p*-type Si) or partial (*n*-type Si) band flattening, to a degree controlled by widely different minority-carrier capture cross section at each interface. The uncompensated charge density at the interface was also calculated from the theory. © *2005 American Institute of Physics*. [DOI: 10.1063/1.1850197]

I. INTRODUCTION

The technique of laser infrared photocarrier radiometry[1,2] (PCR) in Si is believed to be associated with room- or higher-temperature near-infrared photoluminescence, a phenomenon which in the past has invariably been associated with the presence of impurities or defects.[3] Very-low-yield room-temperature photoluminescence has been reported spectroscopically for ion-implanted and doped Si, as well as for the observation of swirl and mechanical defects.[4–7] Unlike those static photoluminescence techniques that require a photomultiplier detector, modulated PCR under lock-in detection has been found to exhibit superior signal-to-noise ratios (on the order of several hundred to several thousand) and to be very sensitive to electronic transport properties of the semiconductor material.[1,2] Unlike conventional photothermal and photoacoustic techniques, PCR is only responsive to the modulated free photoexcited carrier-density-wave (CDW) recombination emissions and completely filters out all thermal infrared (Planck) emissions. This fact makes the technique more sensitive to purely opto-electronic phenomena, eliminating thermal emission interferences and the thermal-noise-limited HgCdTe or other infrared detectors, in favor of photon-noise-limited InGaAs detectors. Therefore, it greatly facilitates signal interpretation by avoiding modeling complications due to several energy conversion pathways from optical to acoustic and/or thermal. Our first applications of PCR to industrial semiconductor Si wafer diagnostics have established the sensitivity of this technique to surface and near-surface electronic recombination effects.[1,2,8,9] Based on the development of a PCR theory of the optical modulation and relaxation of band bending toward photosaturation (flatband condition) at the Si–SiO_2 interface,[10] an appropriate experimental method is introduced in this paper. A harmonically modulated low-intensity superband-gap primary laser beam acts as the PCR signal carrier from the oscillating recombining photoexcited CDW, while a coincident higher-intensity secondary (unmodulated) superband-gap laser beam acts as optical bias and is used as an oxide-semiconductor interface charge occupancy and space-charge layer (SCL) control. As a result, it is found that this combined-laser PCR method can be used to measure the SCL width from fully bent bands (in the dark) to the flatband state, depending on the type (*n* or *p*) of the doping impurity.

[a)] Electronic mail: mandelis@mie.utoronto.ca

The results show that the methodology can be used as a quantitative analytical tool for monitoring and controlling uncompensated interface state charge densities (coverage) and potentially near-surface electronic contamination in an entirely optical remote manner.

II. THEORETICAL MODEL SIMULATIONS

In order to understand the salient features of the present combined *ac*/*dc* laser PCR methodology, a few simulations of the physical aspects of the theory[10] are in order. The general equation for the PCR signals S_P, Eq. 52,[10] is reproduced here for convenience,

$$
\begin{aligned}
S_P(I_0,\omega;\alpha) \cong{}& C_0(R_1,R_2;\alpha_{\mathrm{IR}})\left\{\frac{\eta_Q[1-R_1(\lambda_\alpha)]I_0\alpha}{2h\nu}\right\}\\
&\times\biggl(\frac{T_{ri}(\omega)}{\alpha}\bigl[1-(1+\alpha W_m)e^{-\alpha\Delta W}\bigr]\\
&+\frac{1}{D_n^*(\alpha^2-k^2)}\biggl\{\frac{g}{k(G_2-G_1e^{-2kL})}\\
&\times\bigl[\bigl\{(1+\alpha W_m)-[1+(\alpha-k)W_m]e^{-kL}\bigr\}\\
&\times\bigl(G_2+e^{-kL}\bigr)+[\Delta W-W_m(1-\alpha\Delta W)]\\
&\times\bigl(G_2+e^{-2kL}\bigr)\bigr]-\frac{1}{2\alpha}\bigl[(1+\alpha W_m)-e^{-\alpha L}\bigr]\\
&-\bigl[\Delta W-W_m(1-\alpha\Delta W)\bigr]\biggr\}e^{-\alpha\Delta W}\biggr)e^{i\omega t}. \qquad (1)
\end{aligned}
$$

Here, C_0 is a material depth- and frequency-independent constant. λ_α denotes the wavelength of the excitation radiation. In our experiments, this equation has been applied with superband-gap radiation of absorption coefficient $\alpha(h\nu) > 10^3\ \mathrm{cm}^{-1}$, such that the semiconductor material is entirely opaque to the incident radiation, $e^{-\alpha L}\approx 0$. The quantities g, G_1, and G_2 are given by

$$
g \equiv \frac{S_1+\alpha D_{\mathrm{eff}}}{S_1+k(\omega)D_{\mathrm{eff}}};\quad G_1 \equiv \frac{k(\omega)D_{\mathrm{eff}}-S_1}{k(\omega)D_{\mathrm{eff}}+S_1};
$$

$$
G_2 \equiv \frac{k(\omega)+S_2}{k(\omega)D_n^*-S_2}. \qquad (2)
$$

They are minority CDW interfacial coupling and accumulation/depletion coefficients.[11] $k(\omega)$ is the minority electron CDW wave number (magnitude of the complex wave vector in one dimension) defined as

$$
k(\omega) \equiv \left(\frac{1+i\omega\tau_n}{D_n^*\tau_n}\right)^{1/2}. \qquad (3)
$$

S, D^*, and τ_n stand for CDW transport properties: surface (front: 1; back: 2) recombination velocity, carrier ambipolar (D_n^*) or interface (D_{eff}) diffusion coefficient, and minority (electron) recombination lifetime in *p*-Si, respectively. $T_{ri}(\omega)$ is a complex interface lifetime

$$
T_{ri}(\omega) \equiv \frac{\tau_{ri}}{1+i\omega\tau_{ri}}, \qquad (4)
$$

where τ_{ri} is a charged interface recombination lifetime.[10] The effective SCL width $\Delta W = W_0 - W_m$ and W_m are functions of the incident modulated laser intensity I_0. W_0 and W_m are the dc and modulated components of the SCL,

$$
W(I_0) = W_0 - W_m(I_0)e^{i\omega t}. \qquad (5)
$$

Some simulations of Eq. (1) are now presented with two possible experimental modes in mind. In the simplest configuration, a single modulated superband-gap laser source of variable intensity, I_0, is incident on a $\mathrm{SiO_2}$–Si interface that has a fixed amount of charge, Q_{si} and therefore exhibits band bending with a SCL width of $W_0(Q_{\mathrm{si}})$. The variable intensity laser induces a modulation $W_m(I_0)$ in the SCL width through a change in interface charge coverage, as described by Eq. (5). The structure of Eq. (1) shows that there will be a nonlinear low-intensity range in the dependence of the resulting PCR signal on I_0 up to the flatband value I_{FB} when the SCL will oscillate between the extreme values of W_0 (in the dark) and 0 (full illumination). As the pump-laser intensity increases beyond the value $I_0 = I_{\mathrm{FB}}$, no further dependence of the SCL oscillation amplitude on I_0 is expected, as long as the CDW transport properties remain unchanged and free of nonlinear interactions commonly exhibited in the high-injection limit (10^{18}–$10^{19}\ \mathrm{cm}^{-3}$), such as Auger recombination (Ref. 12, Sec. 1.5.3), carrier–carrier scattering,[13] or band narrowing.[14] Therefore, for $I_0 > I_{\mathrm{FB}}$ the PCR signal would then increase linearly with intensity. These effects have already been observed qualitatively.[1]

In a somewhat more involved experimental configuration, but perhaps simpler signal interpretation, a fixed (low)-intensity modulated ("ac") laser acts as the primary excitation source which produces a fixed density of free electron-hole pair (EHP) carrier waves acting as the PCR probe, and a small fixed-amplitude modulation of the SCL width, $W_m(I_{\mathrm{ac}})$. A coincident unmodulated ("dc") secondary laser source with variable intensity, I_{dc}, substantially exceeding that of the modulated laser but for the lowest values, can change the occupation of the surface states up to complete charge neutralization coverage leading to the flatband condition when $I_{\mathrm{dc}} = I_{\mathrm{FB}}$. In this configuration the dc laser induces a change in the degree of steady band bending at the surface from the dark (maximum) value, $W_0(I_{\mathrm{dc}}=0) = W_{\max}$, of the SCL width up to the flatband (minimum) value, $W_0(I_{\mathrm{FB}}) = 0$. In this ideal picture, the modulated laser is nonperturbing, acting only as a PCR signal carrier with negligible effect on the SCL width, since $W_m(I_{\mathrm{ac}}) \ll W_0(I_{\mathrm{dc}})$. A variation in dc laser intensity within the range $0 \leq I_{\mathrm{dc}} \leq I_{\mathrm{FB}}$ is expected to act as a variable optical bias by means of the steady-state excess recombination events of minority carriers into impurity states. The enhanced steady bulk recombination further affects (increases) the steady SCL minority charge density Q_{si}, driving the $\mathrm{SiO_2}$–Si interface into deeper depletion or inversion. This change alters the (thermo)dynamically coupled interface charge state coverage,[10] causing a concomitant change in the degree of band bending between maximum and zero (flatbands). Because these interface changes perturb the

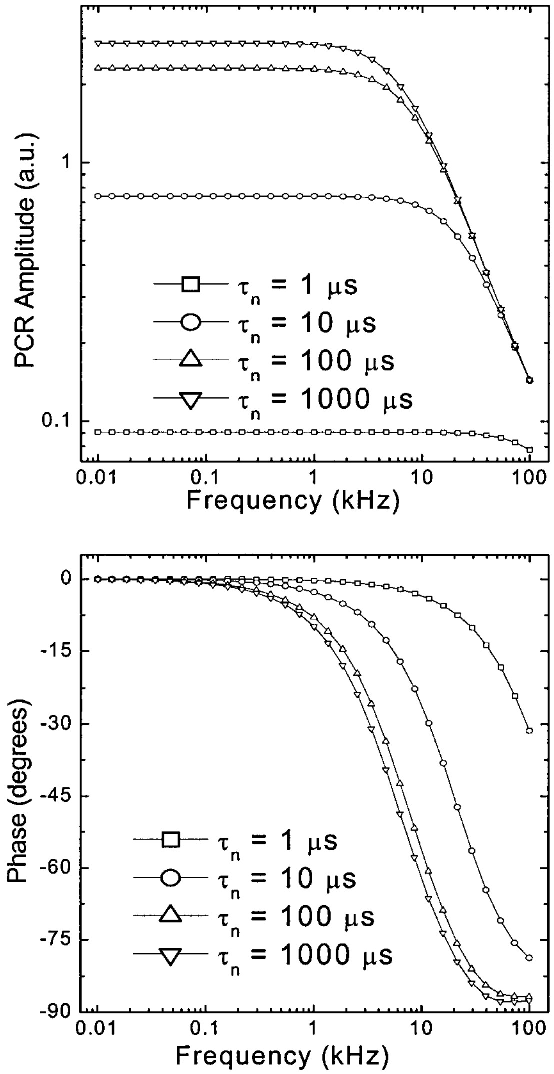

FIG. 1. PCR signal vs modulation frequency simulations for *p*-type Si under flatband conditions ($W_0 = W_m = 0$) with bulk minority CDW recombination lifetime τ_n as a parameter. $S_1 = 300$ cm/s, $S_2 = 10^5$ cm/s, $D_n^* = 30$ cm^2/s, $L = 550$ μm, and α(514 nm) $= 7.76 \times 10^3$ cm^{-1}. (a) Amplitude; (b) phase.

small CDW generated by the modulated laser, the entire process can be described according to Eq. (1), with an effective steady value of $W_0(I_{dc})$ for each I_{dc} value and a fixed $W_m(I_{ac})$.

Given the well-known dependence of the minority free-carrier transport properties on the level of photocarrier injection under unmodulated[15] and modulated[16,17] conditions, the dependence of the PCR signal on the relevant parameters in Si (surface recombination velocities, photocarrier density-wave lifetime, and diffusion coefficient) has been reported under flatband conditions,[1,2] as well as for ion-implanted Si wafers.[8,9] Given that our experimental results in this work were obtained under high-injection conditions with regard to the unmodulated optical bias laser, changes of those parameters with variable laser intensity were observed. To sort out the effects of band bending and of changing transport parameters on the PCR signal, Figs. 1–3 show simulations of the effect of changes in bulk transport properties for a charged SiO$_2$–Si interface exhibiting no band bending using Eq. (1).

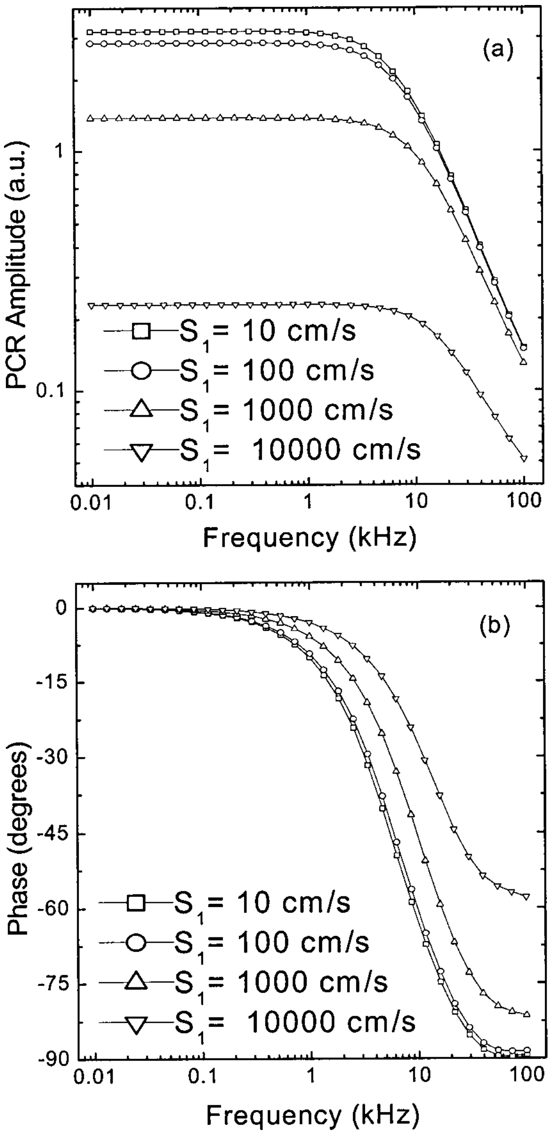

FIG. 2. PCR signal vs modulation frequency simulations for *p*-type Si under flatband conditions ($W_0 = W_m = 0$) with minority CDW interface recombination velocity S_1 as a parameter. $\tau_n = 100$ μs, $S_2 = 10^5$ cm/s, $D_n^* = 30$ cm^2/s, $L = 550$ μm, and α(514 nm) $= 7.76 \times 10^3$ cm^{-1}. (a) Amplitude; (b) phase.

Due to the high value of the optical-absorption coefficient α, it was assumed that the magnitude of $|T_{ri}/\alpha| \ll 1$ and its contribution to Eq. (1) were neglected.

Figure 1 shows a family of frequency curves with minority recombination lifetime variations in the range 1 μs $\leq \tau_n \leq 1$ ms, typical of today's industrial Si wafers. As expected,[1,2] a decrease in τ_n depresses the PCR amplitude and shifts the position of the turning point ("knee") to progressively higher frequencies as the density of the carrier wave over one period decreases with decreasing recombination time. The phases exhibit zero delay with respect to the modulation source at low frequencies, such that $\omega\tau_n \ll 1$, but they begin to lag behind the source phase as soon as this condition is not valid. As τ_n decreases, the foregoing condition becomes violated at progressively higher frequencies, whence the shift of the PCR phases in Fig. 1(b).

Figure 2 shows the PCR frequency behavior with SiO$_2$–Si interface recombination velocity, S_1, as a parameter.

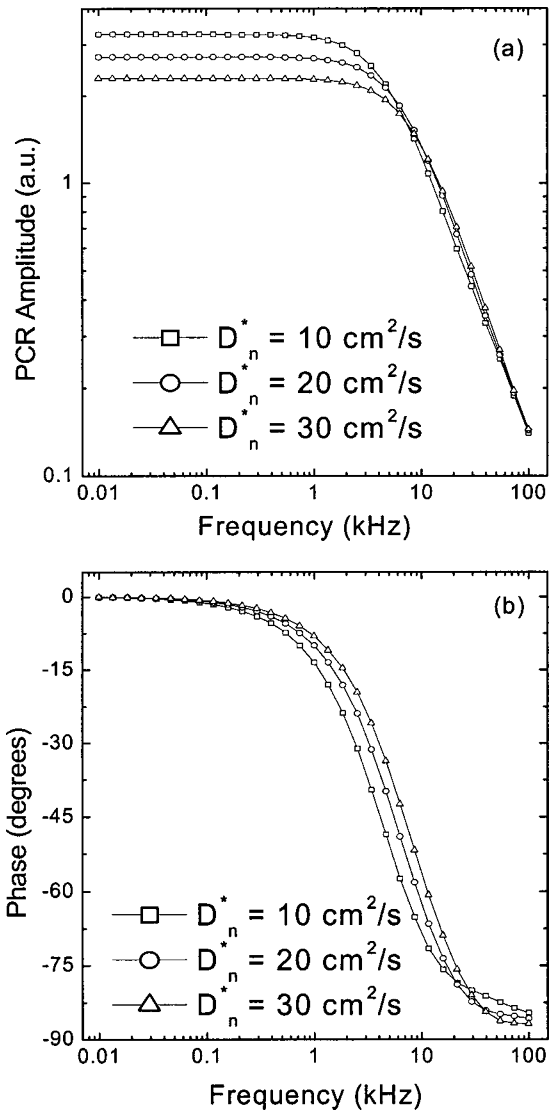

FIG. 3. PCR signal vs modulation frequency simulations for *p*-type Si under flatband conditions ($W_0=W_m=0$) with ambipolar diffusivity D_n^* as a parameter. $\tau_n=100\ \mu\text{s}, S_1=300\ \text{cm/s}, S_2=10^5\ \text{cm/s}, L=550\ \mu\text{m}$, and $\alpha(514\ \text{nm})=7.76\times10^3\ \text{cm}^{-1}$. (a) Amplitude; (b) phase.

Increasing S_1 by several orders of magnitude has effects quite similar to decreasing τ_n, although the knee shift to higher frequencies is not as pronounced. Similarly, the onset of the PCR phase lag moves to higher frequencies and shows the familiar saturation[1] at a progressively decreasing phase lag with increasing S_1, because the subsurface ac diffusion length (or "centroid") of the CDW, the inverse of the wave number Eq. (3), is no longer controlled by the bulk recombination lifetime τ_n alone. Instead, it becomes controlled by an *effective* lifetime, τ_{eff}, such that,[18]

$$\frac{1}{\tau_{\text{eff}}}=\frac{1}{\tau_p}+\frac{1}{\tau_s}, \tag{6}$$

where τ_s is the interface lifetime (Ref. 10; Appendix) related to the interface recombination velocity S_1. This time constant begins to influence the effective lifetime (and hence the phase saturation level) at S_1 values such as $\tau_s\sim\tau_n$.

Figure 3 shows the effect of changing ambipolar diffusivity on the frequency scans. It is clear that when the semiconductor bulk controls D_n^*, an increase in that quantity amounts to decreasing PCR amplitude because the CDW centroid shifts away from the detection point at the surface/interface, with the result that the overall free-carrier density decreases as the effective CDW thickness (subsurface spread) controlled by the minority-carrier ac diffusion length $L_n(\omega)=k^{-1}(\omega)$ increases. The onset of the PCR phase lag and its steepest slope also exhibit a shift to higher frequencies with increasing D_n^* consistently with Eq. (3), which shows that the position of the CDW centroid can be shifted to a smaller depth by increasing frequency to compensate for the increased D_n^*.

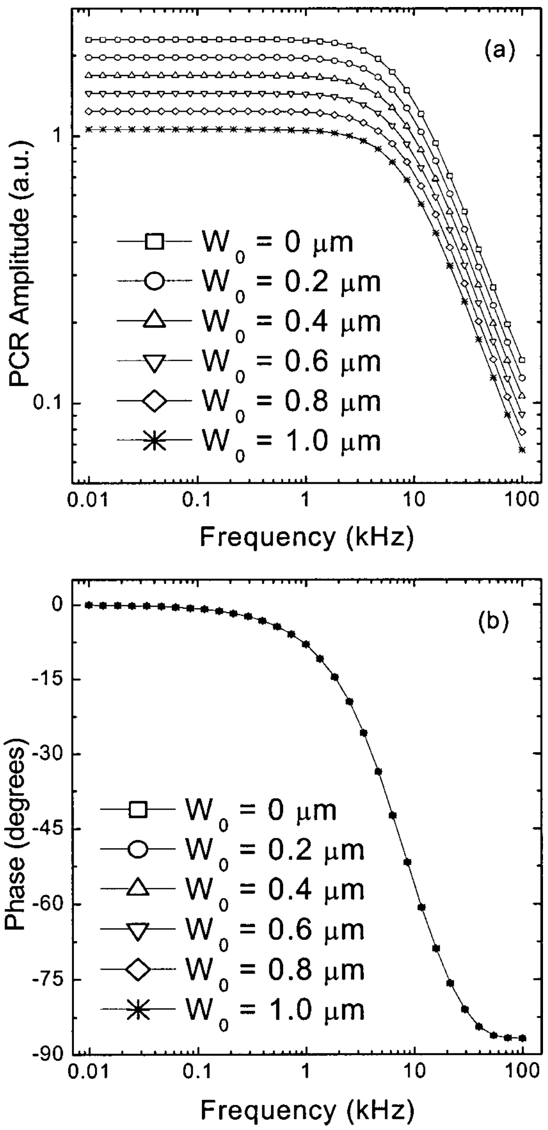

FIG. 4. PCR signal vs modulation frequency simulations for *p*-type Si with constant transport parameters and with the SCL width as a parameter. $W_m=0, D_n^*=30\ \text{cm}^2/\text{s}, \tau_n=100\ \mu\text{s}, S_1=300\ \text{cm/s}, S_2=10^5\ \text{cm/s}, L=550\ \mu\text{m}$, and $\alpha(514\ \text{nm})=7.76\times10^3\ \text{cm}^{-1}$. (a) Amplitude; (b) phase.

Figures 4 and 5 show the effects of nonzero band bending on the PCR signal. Assuming negligible W_m for low intensity of the modulated laser compared to W_0, Fig. 4, it is seen that increasing W_0, with the transport parameters of Figs. 1–3 kept constant, results in a monotonically decreasing amplitude and essentially no change in phase. This be-

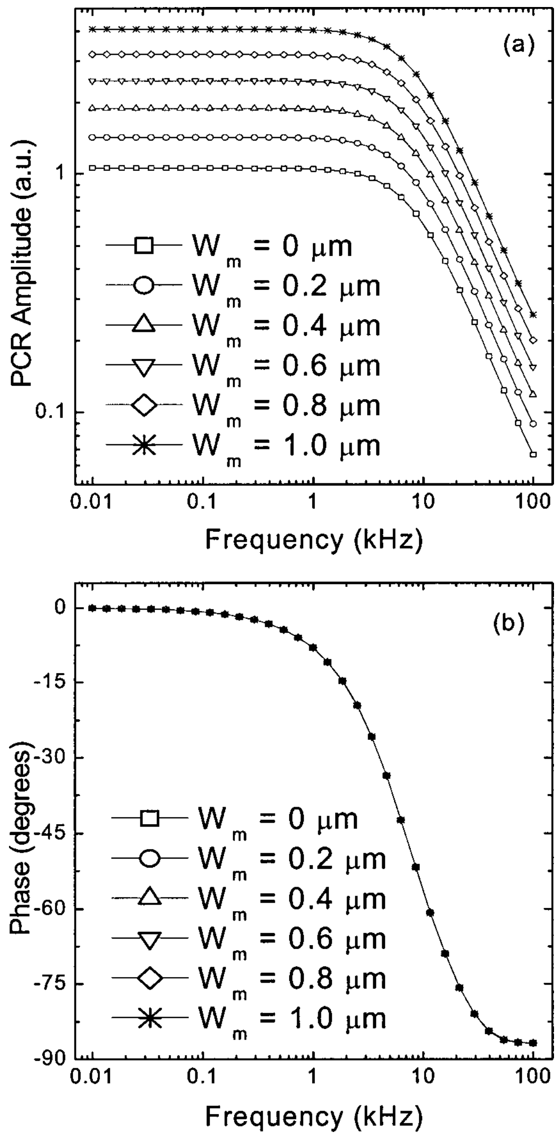

FIG. 5. PCR signal vs modulation frequency simulations for *p*-type Si with constant transport parameters and with the optically modulated SCL width, W_m, as a parameter. $W_0=1\ \mu\mathrm{m}, D_n^*=30\ \mathrm{cm}^2/\mathrm{s}, \tau_n=100\ \mu\mathrm{s}, S_1=300\ \mathrm{cm/s}, S_2=10^5\ \mathrm{cm/s}, L=550\ \mu\mathrm{m}$, and $\alpha(514\ \mathrm{nm})=7.76\times 10^3\ \mathrm{cm}^{-1}$. (a) Amplitude; (b) phase.

havior is expected since an increased degree of band bending is the result of increased interface charge density in the model and thus higher trap density and loss of free carriers. The process takes place right at the Si–SiO$_2$ interface where free minority carriers deexcite mostly nonradiatively in trap states over the space-charge barrier[19] and therefore are not available to contribute to the PCR signal through radiative NIR emissions. Furthermore, there is no measurable phase shift because the interface recombination lifetime τ_s was assumed constant. This simplification turns out not to be true experimentally, but the simulation points out the important fact that it is *not* the value of W_0 itself that causes a phase shift, but rather the effect that a change in this value has on the transport properties at the Si–SiO$_2$ interface. Figure 5 corresponds to the case where the maximum value, W_0, of the SCL width is fixed, but is subject to oscillating amplitude, W_m, which increases with, e.g., increasing intensity of the modulated laser source. As expected, the PCR amplitude increases as the modulated band curvature tends to offset the effect of the CDW-inhibiting band bending through more effective neutralization of the interface charges over the modulation cycle. As a result, a higher density of free minority carriers can survive over one illumination period and contribute radiatively to the increased PCR signal. As in the case of Fig. 4(b), the phase does not show any change over the entire range of W_m values used in this simulation. When the changes in the SCL widths, Figs. 4 and 5, and in transport parameters, Figs. 1–3, are combined in a frequency plot for fixed values of the transport parameters, it is found that the former simply shifts the PCR amplitude accordingly, while the phase remains fixed. This conclusion proves to be very helpful in interpreting experimental PCR measurements of the SCL.

Figures 6 and 7 show simulations of the PCR signals using the combined technique of superposing a modulated PCR pump laser with a dc optical bias laser. For fixed modulation frequency and amplitude, and assuming a simple exponential dependence of the SCL width on I_{dc}, a scan of the intensity I_{dc} produces PCR amplitude curves which photosaturate when $I_{\mathrm{dc}} \sim I_{\mathrm{FB}}$. The effects of changing bulk minority recombination lifetime are shown in Fig. 6, and those of changing interface recombination velocity are shown in Fig. 7. In both cases the shapes of the amplitude curves, $A(I_{\mathrm{dc}})$, are similar. The phases, $\phi(I_{\mathrm{dc}})$, remain flat, for the same reasons as in Figs. 4(b) and 5(b). However, the difference $A(I_{\mathrm{FB}})-A(0)$, where I_{FB} is measured at the lowest photosaturation value of I_{dc}, increases with increasing τ_n and with decreasing S_1, and the relative phase lag $\phi(I_{\mathrm{FB}})-\phi(0)$ increases, respectively, as the centroid of the CDW moves deeper into the bulk. These observations lead to the important conclusion that the effects of SCL band bending at the Si–SiO$_2$ interfaces become progressively more detrimental to the near-surface optoelectronic behavior of semiconductors with today's high-quality carrier transport parameter values, such as high-resistivity Si substrates and epitaxial thin films.

III. MATERIALS, EXPERIMENTS, AND RESULTS

Four- and six-inch 5–10 Ω cm, 550-μm-thick, *p*-type Si wafers were oxidized with a gate oxide of ca. 1000 Å. In addition, *n*-type wafers were also oxidized with ca. 5000-Å oxide. The photocarrier radiometry setup is shown in Fig. 8. The two-laser configuration described in Sec. II was used for SCL measurements. The modulated low-power laser was either a He–Ne laser (632.8 nm; 0.4-mm beam radius) or a GaAlAs laser diode (830 nm; 0.30-mm beam radius). The unmodulated optical bias laser was an Ar-ion laser (514 nm; 1.89-mm beam radius). The various beam radii were characterized using a pinhole-on-detector system scanned across the beam profile with a neutral density filter to avoid photodetector saturation. The IR detector was a switchable-gain InGaAs element (ThorLabs model PDA400), 1-mm in diameter, with spectral response in the 800–1750 nm range, peak response at 1550 nm, and frequency bandwidth from dc to 10 MHz. The preamplifier was incorporated into the detector housing, a design which delivered optimal signal-to-noise

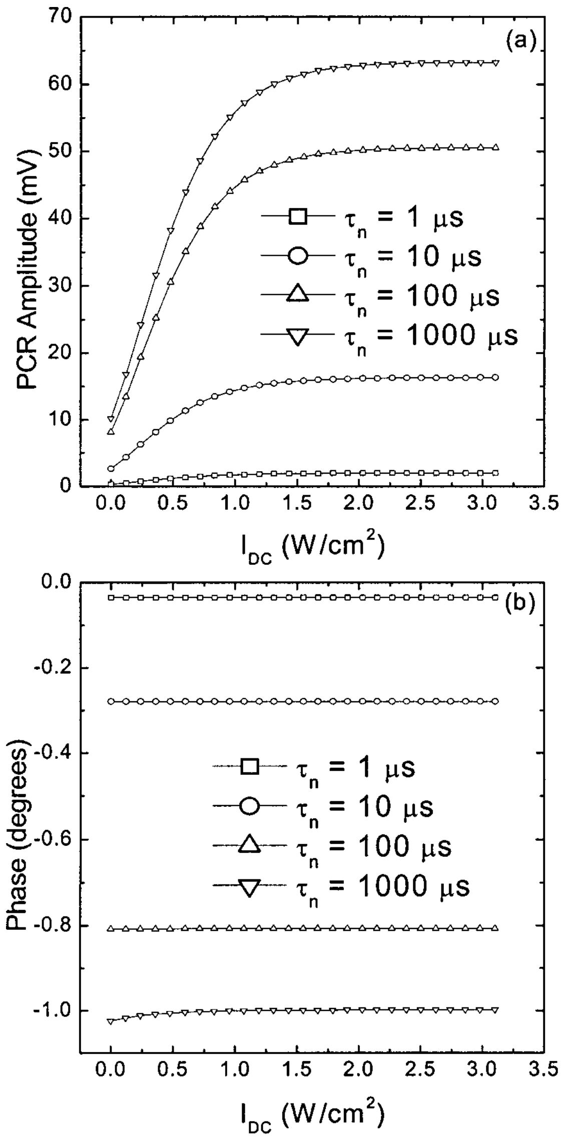

FIG. 6. (a) Amplitude; (b) phase of the PCR signal vs dc optical bias laser intensity I_{dc} simulations for *p*-type Si with constant transport parameters, a small fixed-amplitude optically modulated SCL width $W_m=0.2\ \mu$m, and with τ_n as a parameter. $D_n^*=30\ \mathrm{cm^2/s}, S_1=300\ \mathrm{cm/s}, S_2=10^5\ \mathrm{cm/s}, L=550\ \mu$m and $\alpha(514\ \mathrm{nm})=7.76\times 10^3\ \mathrm{cm^{-1}}$. A simple exponential dependence of the SCL width on I_{dc} was assumed in Eq. (1), $\Delta W\equiv W_0-W_m=A\exp(-BI_{dc})$.

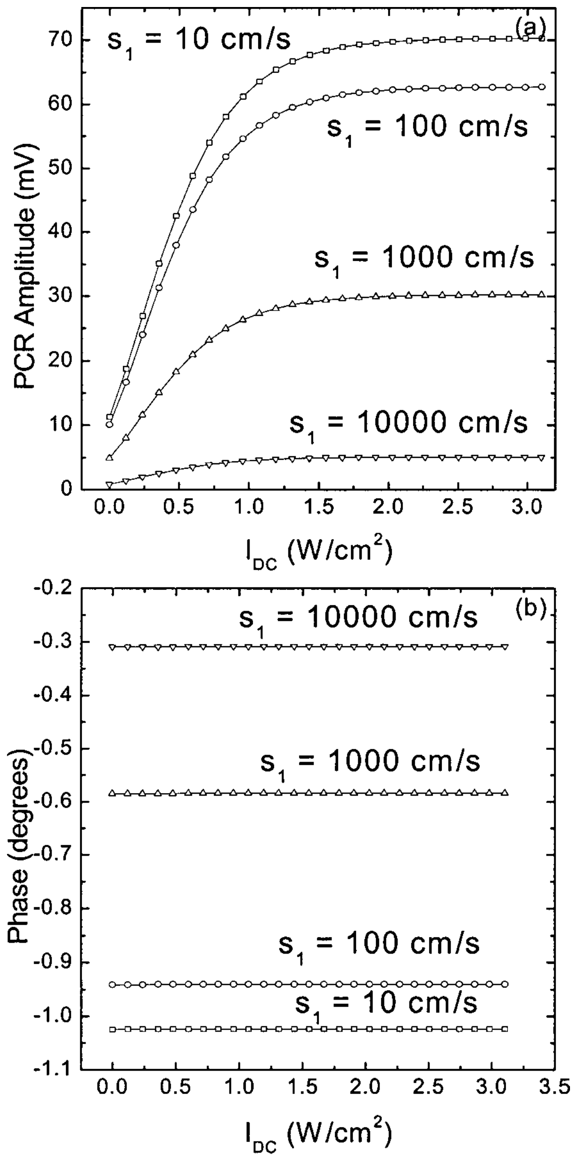

FIG. 7. Similar to Fig.6 with $\tau_n=100\ \mu$s and S_1 as a parameter.

ratio expressed as a noise equivalent power (NEP) figure of $2.9\text{–}8.2\times 10^{-12}\ \mathrm{W}/\sqrt{\mathrm{Hz}}$. The detector was outfitted with a specialty long-pass optical filter from Spectrogon featuring steep cut on (5% at 1010 nm, 78% at 1060 nm), and transmission range of 1042–2198 nm. The cut-on quality of the filter is crucial in PCR as it must block any synchronous pump radiation leakage from reaching the highly sensitive detector. Short-wavelength filtering of optical density five or six is usually required. The samples were placed on an aluminum backing which acted as a mechanical support and signal amplifier by redirecting the forward emitted IR photons back toward the detector,[1] Fig. 8. Typical modulated power used was $P_{ac}\sim 0.5\text{–}4$ mW, whereas the power of the unmodulated laser was varied up to 350 mW. Taking into account the reflectivity of Si at 514 nm at normal incidence ($R=0.38$) and the laser beam radius $r=1890\ \mu$m, the effective maximum photon flux at 350 mW was $F_{p,\max}=1.103\times 10^{19}\ \mathrm{photons/cm^2\,s}$. According to Jastrzebski *et al.*,[17] this range of photon flux is appropriate and required (10^{17}–$10^{18}\ \mathrm{photons/cm^2\,s}$) to drive the depletion-level interface barrier height and the surface photo voltage (SPV)

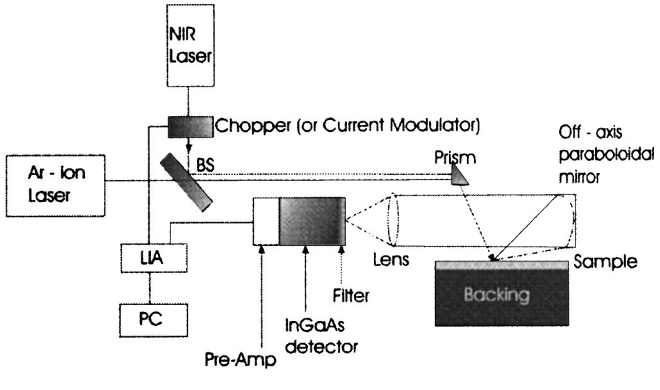

FIG. 8. Experimental PCR setup showing the modulated and unmodulated lasers for space-charge layer investigations.

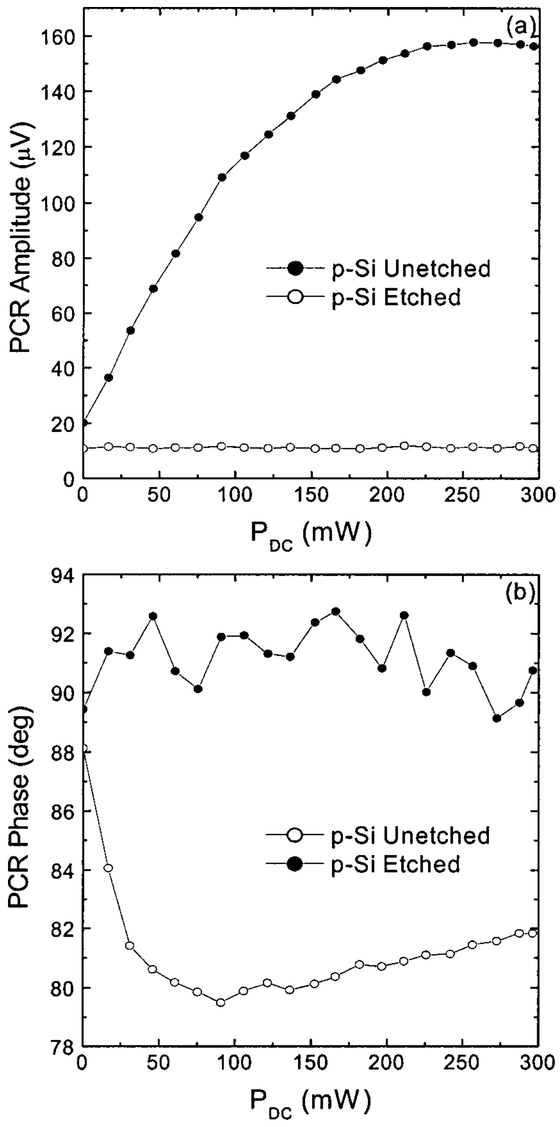

FIG. 9. (a) Amplitudes and (b) phases of an oxidized *p*-Si wafer before and after etching the SiO_2 away. The modulated beam was provided by a mechanically chopped He–Ne laser. Chopping frequency, 200 Hz.

(alternately, PCR) signal, to the flatband condition. Assuming unity optical-to-ehp photon energy conversion efficiency, it is important to note that the maximum free-carrier flux in our experiments was

$$F_e = \frac{3.43 \times 10^{17}}{\pi(r + \sqrt{D_n \tau_n})^2} = 1.13 \times 10^{18} \text{ electrons/cm}^2\text{ s}, \qquad (7)$$

where the dc minority diffusion length $L_n = \sqrt{D_n \tau_n} = 0.122$ cm for typical values of $D_n \sim 30$ cm^2/s and $\tau_n \sim 500$ μs according to our results for *p*-Si–SiO_2 interfaces, Figs. 15 and 16. Therefore, the experiments were conducted in the high-injection regime.[15]

Some wafers were exposed to variable optical bias with the laser beam incident on the SiO_2 and then were etched to hydrophobia in an aqueous solution of 10 vol % HF in water, indicating that the SiO_2 layer was fully removed. The PCR signal amplitudes and phases of a *p*-Si sample before and after etching are shown in Fig. 9. While the oxidized wafer exhibits complete photosaturation at irradiation with ~250 mW of continuous laser power, it is clear that the removal of the oxide also removed the interface-charge layer very efficiently while increasing the nonradiative electron trapping efficiency at the etched surface. Accordingly, the PCR amplitude dropped significantly and remained independent of the power of the unmodulated laser. The Ar-ion laser-beam reflectance of the wafer before and after etching was measured to be 0.340 and 0.408, respectively. The reflectance of the primary He–Ne beam was 0.295 and 0.339, respectively. These differences cannot account for the drastic change in the PCR amplitude after etching, giving further support to enhanced nonradiative recombination. The PCR phase, Fig. 9(b), shows a very reproducible curvature for the oxidized sample. On the other hand, the phase of the etched sample is independent of P_{dc} and became noisier due to the low signal associated with this sample. Signal-to-noise ratios (SNR) for oxidized wafers were in the 100–200 range with error bar sizes similar to the symbol size used in the plots, whereas those for the etched samples were ~18–25. The photosaturation exhibited by the PCR amplitude of the unetched sample of Fig. 9(a) is similar to the one reported under surface photovoltage probing by Jastrzebski *et al.*[17] Those authors qualitatively attributed the photosaturation to the attainment of the flatband condition under external optical bias.

The issue of possible perturbation effects of the primary modulated laser beam on the SCL measurements was investigated by changing the power of the He–Ne laser and repeating the experiment of Fig. 9 using another oxidized *p*-Si wafer. Typical results are shown in Fig. 10. As expected, the PCR signal amplitude does scale with P_{ac} (or, equivalently, I_0), Eq. (1); however, the rescaled amplitude of the measurement with decreased power of 1.4 mW coincides with the 3.5-mW amplitude, when normalized to the highest point of the latter curve. Similarly, the phases coincide with no rescaling within the error, with the phase obtained at the lower power exhibiting higher noise. These results demonstrate that, in the range of the reported measurements, the modulated laser was nonperturbing of the electronic properties of the semiconductors and the observed signal variations with P_{dc} were due solely to the effects of the dc laser on the sample.

Figure 11 shows that the effects of surface polishing on the PCR signal from the *p*-type wafer of Fig. 10 (amplitudes and phases) are minor. The back matte surface was also oxidized and therefore it was expected that it would exhibit a SCL behavior similar to the front surface. Based on the fits to the theory as described below, these effects can be accounted for by small differences in the respective surface recombination velocity, effective lifetime, and SCL depth profile.

The SCL profile for the *n*-type Si wafers was also investigated. Typical results are shown in Fig. 12. Both lasers were incident on the exposed SiO_2 layer. In all cases, large differences were observed in the PCR amplitudes between intact and etched samples. Nevertheless, there was no indication of flatband saturation within the range of I_{dc} intensities available and phases were always essentially independent of the dc laser power. A comparison between the amplitude shapes and absolute signal levels in Figs. 9 and 12 shows

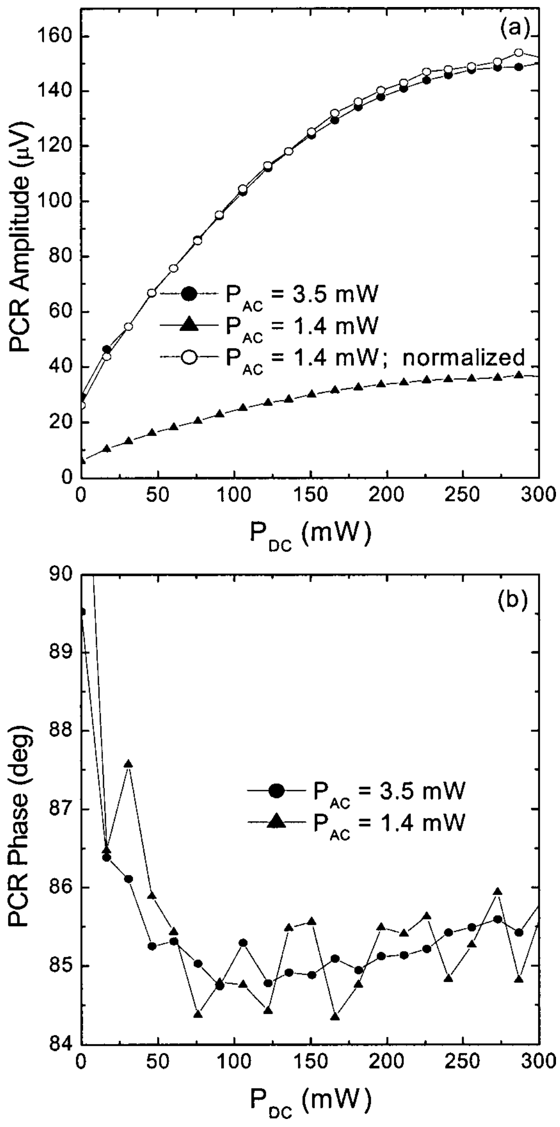

FIG. 10. (a) Amplitudes and (b) phases of an oxidized *p*-Si wafer using two different power levels of the primary (modulated) laser beam. He–Ne laser chopping frequency, 200 Hz.

that it is much harder for the optical bias to induce complete flattening of the bands in *n*-Si than in *p*-Si. This observation indicates the relatively low efficiency of this methodology for driving *n*-Si into the flatband state. The independence of PCR phases from I_{dc} is an additional indicator that the optical bias does not affect the transport properties of the $\mathrm{SiO_2}$–*n*-Si interface.

The developed PCR theory[10] resulting in Eq. (1) was tested through a series of PCR measurements with Si–$\mathrm{SiO_2}$ interfaces, which were aimed at reconstructing the depth profile of the SCL from scans of I_{dc} at a fixed frequency. Results on a *p*-Si sample, such as those shown in Figs. 9–11, were supplemented by frequency scans launched at several values of I_{dc}, as shown in Fig. 13. The individual frequency scans were fitted to Eq. (1) with $\Delta W = W_0$ since the I_{ac} intensity was too low compared to I_{dc} to affect the band bending, as demonstrated in Fig. 10. The fitted parameters at each value of I_{dc} included $\tau_{\mathrm{eff}}, S_1, S_2, D_{\mathrm{eff}} \approx D_n^*$, and W_0. A computational multiparameter feedback program was generated. In the multiparameter fitting process, the following square variance was minimized:

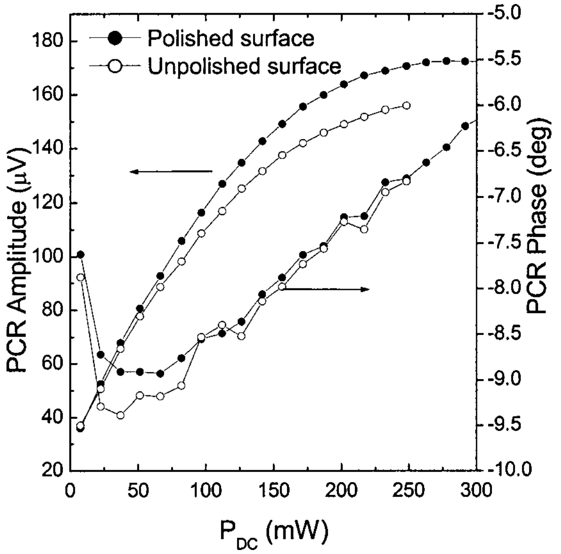

FIG. 11. Effects of surface polishing on the PCR signal amplitude and phase. He–Ne laser chopping frequency, 200 Hz.

$$\mathrm{Var} = \frac{\sum_{m=1}^{N}[A^T(f_m) - A^S(f_m)]^2}{N} + \frac{\sum_{m=1}^{N}[\Phi^T(f_m) - \Phi^S(f_m)]^2}{\sum_{m=1}^{N}[\Phi^S(f_m)]^2}. \tag{8}$$

Here $A^S(f_m)$ and $\Phi^S(f_m)$ are the PCR amplitude and phase, respectively, simulated with the model of Eq. (1), and $A^T(f_m)$ and $\Phi^T(f_m)$ are the associated fitted experimental PCR amplitude and phase. N is the total number of data points. During the fitting procedure, the four transport properties

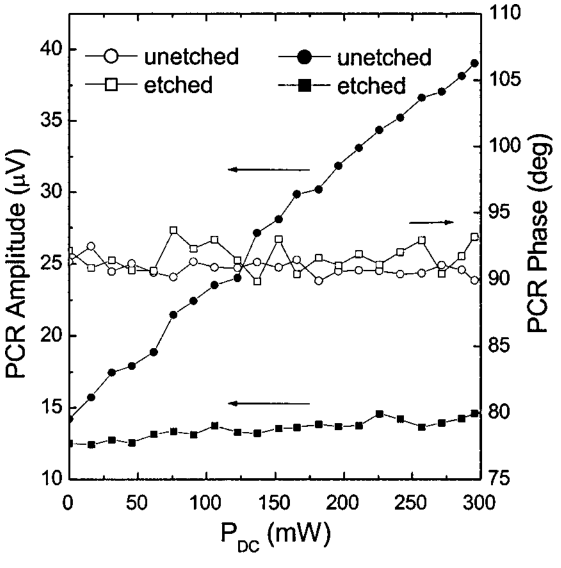

FIG. 12. Amplitudes and phases of an oxidized *n*-Si wafer before and after etching the $\mathrm{SiO_2}$ away. The modulated beam was provided by a mechanically chopped He–Ne laser chopping frequency, 200 Hz.

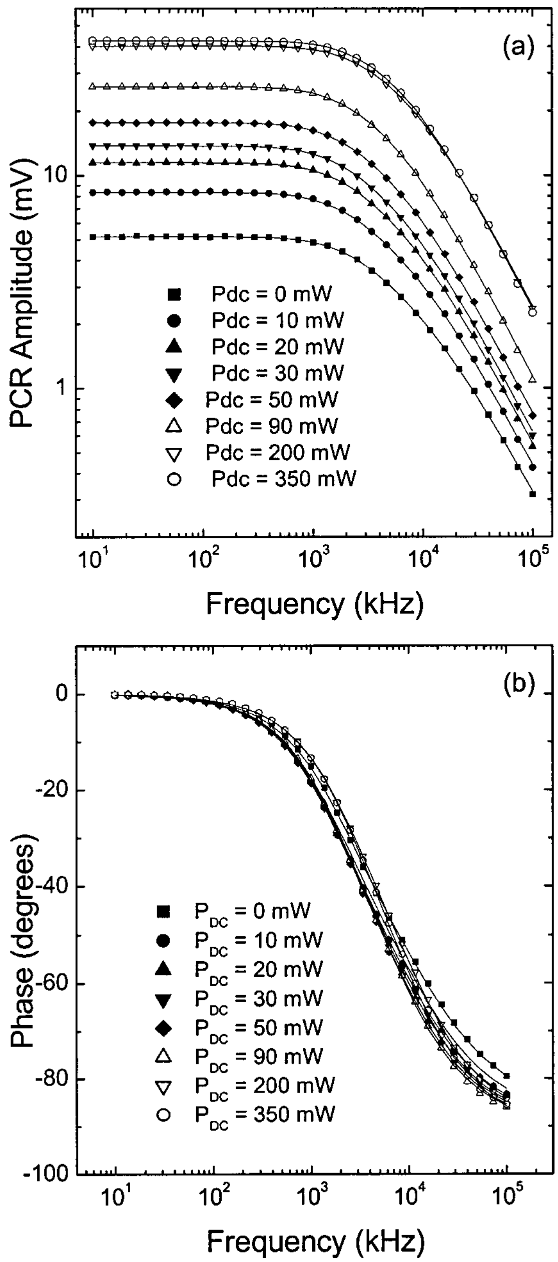

FIG. 13. Amplitude (a) and phase (b) frequency scans of a *p*-Si–SiO$_2$ interface from the polished surface of Fig. 9, under various dc laser power levels and 830-nm modulated excitation source. Theoretical fits to Eq. (1) are indicated by the continuous lines. Unique best fits were determined by the set of parameters $W_0, \tau_{\mathrm{eff}}, S_1, S_2$, and D_{eff} yielding the minimum variance in Eq. (8). For all fits it was found that $0.86\% < \mathrm{Var} < 1.14\%$.

$\tau_{\mathrm{eff}}, S_1, S_2$, and D_{eff} were set as free parameters. The best-fitting procedure commenced at $I_{\mathrm{dc}} = I_{\mathrm{FB}}$, where $W_0 = 0$. Then the first nonzero value of W_0 was incremented for the next lower I_{dc} and all five parameters were allowed to vary until the absolute minimum of Eq. (8) was attained. The values of the five parameters yielding the absolute minimum in Eq. (8) were unique in each case within the physically expected value ranges, and fitting errors were recorded. The procedure was repeated for all $I_{\mathrm{dc}} \geqslant 0$. Figure 14 shows the I_{dc} dependence of the front surface (interface) recombination velocity, S_1, in the range used in our experiments. The decrease of this parameter essentially down to zero is consistent with the physical process of optical neutralization of the interface states by photoexcited minority electrons. The results are also consistent with earlier derived dependencies of the front surface recombination velocity (SRV) on the excess electron density in optically biased photoconductance-decay experiments[20,21], from surface photovoltage measurements using negative corona charging[21], and from basic Shockley–Reed recombination theory.[16,22] Using the dependence $\tau_s = \mathrm{const}(S_1^{-1})$ (Ref. 10; Appendix Eq. A5) results in an increase of the interface recombination lifetime with incident dc laser power. Figures 15 and 16 show the I_{dc} dependencies

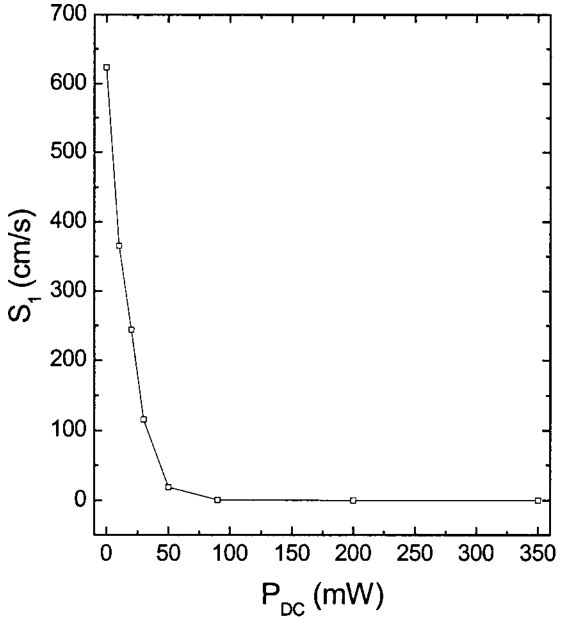

FIG. 14. Recombination velocity for a *p*-Si–SiO$_2$ interface as a function of the Ar-ion laser dc power of a *p*-Si–SiO$_2$ interface. Data obtained from simultaneous best fits to amplitude and phase frequency scans shown in Fig. 13.

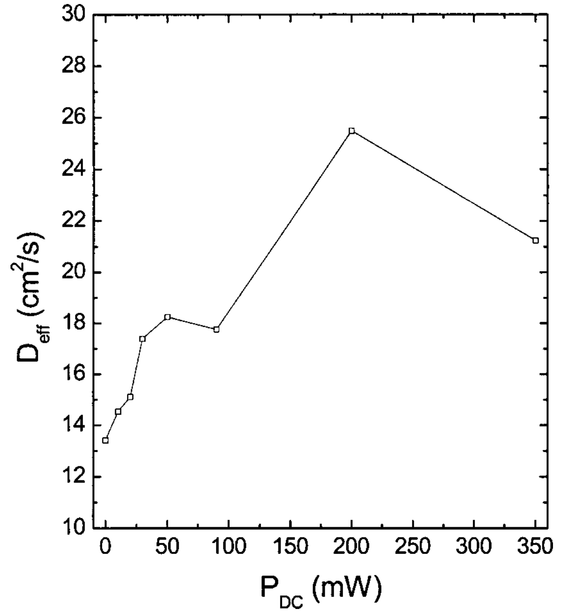

FIG. 15. Effective diffusion coefficient of the carrier density wave as a function of the Ar-ion laser dc power of a *p*-Si–SiO$_2$ interface. Data obtained from simultaneous best fits to amplitude and phase frequency scans shown in Fig. 13.

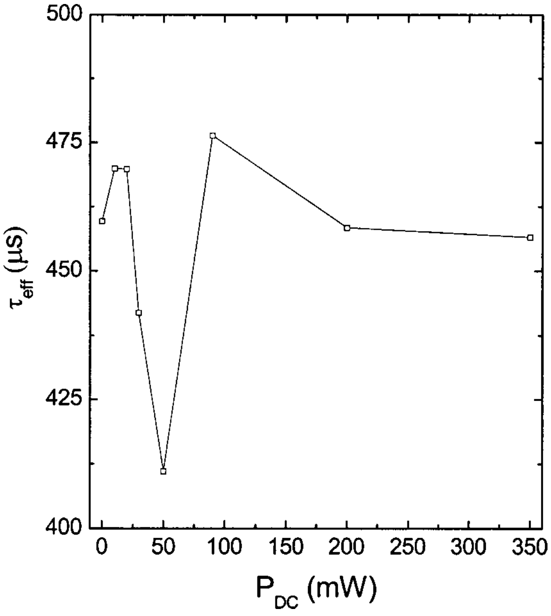

FIG. 16. Effective lifetime of the carrier density wave as a function of the Ar-ion laser dc power of a p-Si–SiO$_2$ interface. Data obtained from simultaneous best fits to amplitude and phase frequency scans shown in Fig. 13.

of the CDW effective diffusion coefficient $D_{\rm eff}$ and effective recombination lifetime $\tau_{\rm eff}$. In the high dc-power range, $P_{\rm dc} > 100$ mW, Fig. 14 shows that $S_1 \approx 0$. Therefore, in that range, according to Appendix Eq. A7 of Ref. 10,

$$\frac{1}{\tau_{\rm eff}} = \frac{1}{\tau_B} + \frac{1}{\tau_s}, \qquad (9)$$

$\tau_{\rm eff} \simeq \tau_B \simeq 460$ μs, a constant value reflecting purely bulk recombination and consistent with Fig. 16. Here τ_B is the bulk recombination lifetime. Nevertheless, for the same $P_{\rm dc}$ range the effective diffusion coefficient of the CDW decreases from an essentially electron minority-carrier diffusivity value of 26 cm^2/s following a relatively steep increase. The onset of decrease at high optical bias corresponds to photoexcited carrier densities of 10^{17} cm^{-3} [calculated from Eq. (7) for excitation at 830 nm] and is consistent with the onset of nonnegligible carrier–carrier scattering reported for Si(111) surfaces.[23] The increase of $D_{\rm eff}$ at low $P_{\rm dc}$ bias power is the result of the ambipolar nature of $D_{\rm eff} \approx D_n^*$ (Ref. 10, Appendix) as the free-electron CDW increases in the near-interface region with increased optical interface charge neutralization, thus changing the value of the ambipolar diffusivity from the majority D_p(~12 cm^2/s) to the minority D_n(~30 cm^2/s) range. The minimum in the value of $\tau_{\rm eff}$ around $P_{\rm dc} = 50$ mW, Fig. 16, is most likely associated with the increasing values of $D_{\rm eff}$ and τ_s; the IR emitting photocarrier density wave shifts to deeper subinterface locations, in agreement with the increased PCR phase lag in Figs. 9(b), 10(b), and 11, and this results in the disappearance of a number of contributing carriers from the field of view of the IR detector.[24] The computational application of Eq. (1) interprets this relative scarcity of carriers as a decreased recombination lifetime. At higher $P_{\rm dc}$ the flattening bands bring about an increased free-carrier density wave in the immediate subinterface region [decreased phase lag in Figs. 9(b), 10(b), and 11] which restores the CDW infrared photon emission within the range of the InGaAs visibility solid angle. The effects of finite detector size on the PCR signal are currently under further investigation along the lines of similar considerations in photothermal radiometry of semiconductors.[24]

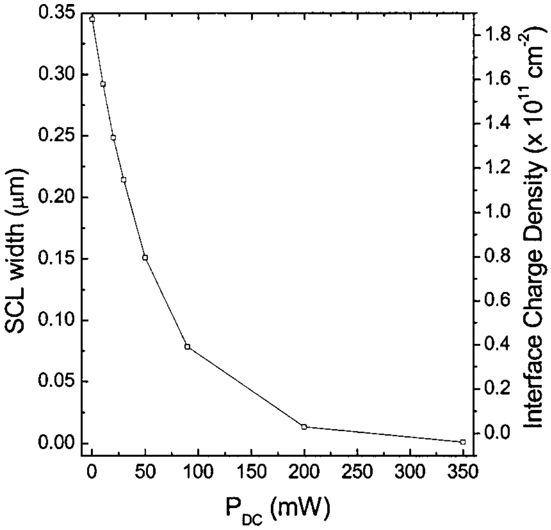

FIG. 17. SCL width of a p-Si–SiO$_2$ interface as a function of the Ar-ion laser dc optical bias. The reconstruction was obtained from simultaneous best fits to amplitude and phase frequency scans shown in Fig. 13. The right axis shows the effective density of non-neutralized interface charges, Eq. (10).

Figure 17 is the reconstructed depth profile of the SCL width from full band bending to the complete flatband condition associated with photosaturation of the PCR signal. Furthermore, the doping density, n_{p0}, at room temperature was estimated from the resistivity of the particular p-Si wafer[25] and was used in[10]

$$N_t - N_{t0}{}^{(r)} = n_{p0} W_0 \qquad (10)$$

to calculate the effective density of non-neutralized interface charges, $N_t - N_{t0}{}^{(r)}$. Although a single interface energy state E_t has been assumed throughout, it is clear that the calculated charge density of Eq. (10) can be generalized to the following distributions:

$$N_t - N_{t0}{}^{(r)} \Rightarrow \sum_d (N_t{}^d - N_{t0}{}^d) \quad \text{for discrete states}, \qquad (11a)$$

$$N_t - N_{t0}{}^{(r)} \Rightarrow \int_d [N_t(E_d) - N_{t0}(E_d)] dE_d \quad \text{for continuous states}. \qquad (11b)$$

Finally, Fig. 18 shows the change in the SCL width of the n-type interface of Fig. 12. Since there was no saturation of the PCR signal possible for the n-type Si wafers, the flatband condition could not be attained and therefore no fully neutralized charge-state signal was available to use as a reference interface state with Eq. (1). Instead, the differential (relative) SCL width $\Delta W_0(I_{\rm dc})$

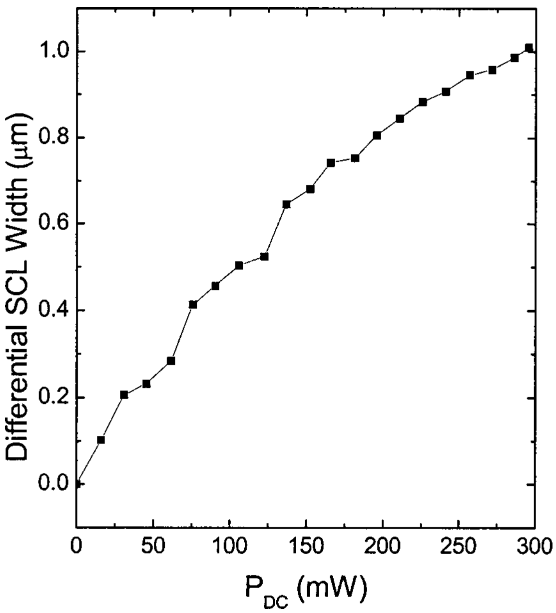

FIG. 18. Relative $\Delta W_0(I_{dc})$ depth profile, Eq. (12), of an n-Si–SiO$_2$ interface as a function of the Ar-ion laser dc optical bias. The reconstruction was obtained from the amplitude of the data in Fig. 12.

$$\Delta W_0(I_{dc}) \equiv W_0(0) - W_0(I_{dc}) = \frac{1}{\alpha}\ln\left[\frac{S_P(I_{dc},\omega;\alpha)}{S_P(0,\omega;\alpha)}\right] \qquad (12)$$

was measured. It is observed that photosaturation is likely for optical bias substantially higher than the maximum 300 mW used in this experiment. The relative inability of the dc optical bias to neutralize the interface charge density in n-Si is due to the much lower (ca. 100 times[16]) hole capture cross section of this type of semiconductor than the respective electron capture cross section in p-Si. This fact leads to much shorter interface lifetimes, τ_s (Ref. 10, Appendix), making it harder for an optical source to build up the neutralized interface charge coverage observed with p-Si–SiO$_2$ interfaces, Fig. 17. The same effect makes the interface recombination velocity essentially independent of excess carrier density at the n-Si–SiO$_2$ interface[16] which results in the independence of the PCR phase from P_{dc}, Fig. 12.

IV. CONCLUSIONS

The interface modulated-charge-density theory developed elsewhere[10] was used for physical simulations involving PCR signals in order to study the effects of the various SCL optoelectronic transport parameters on the PCR amplitude and phase signal channels. Furthermore, an experimental configuration was used involving n- and p-doped Si–SiO$_2$ interfaces and a low-intensity (nonperturbing) modulated laser source as well as a coincident dc laser of variable intensity acting as interface-state neutralizing optical bias. The application of the theory to the experiments yielded the various transport parameters of the samples as well as the depth profile of the SCL. It was shown that PCR can monitor the complete flattening of the energy bands at the interface of p-Si–SiO$_2$ with dc optical powers up to 300 mW. The uncompensated charge density at the interface was also calculated from the theory. With n-Si–SiO$_2$ it proved to be more difficult to flatten the energy bands as expected from the much lower minority-carrier capture cross section of the n-type interface. The present two-laser PCR method is capable of quantitative and contactless depth profilometry of the SCL at intermediate stages of its dynamic optical flattening up to the flatband state.

ACKNOWLEDGMENTS

One of the authors (A.M.) is grateful to the Alexander von Humboldt Foundation for a Research Award that made this work possible. We wish to acknowledge the valuable technical assistance of Dietmar Krüger with sample holder assembly design. The assistance of Dr. Bincheng Li with FORTRAN software for the computational implementation of the theory is gratefully acknowledged. We thank Professor Andreas Wieck for use of his facilities to perform wafer etching.

[1] A. Mandelis, J. Batista, and D. Shaughnessy, Phys. Rev. B **67**, 205208 (2003).
[2] J. Batista, A. Mandelis, and D. Shaughnessy, Appl. Phys. Lett. **82**, 4077 (2003).
[3] G. Lasher and F. Stern, Phys. Rev. **133**, A553 (1964).
[4] C. G. Kirkpatrick, J. R. Noonan, and B. G. Streetman, Radiat. Eff. **30**, 97 (1976).
[5] H. Nakashima, Y. Shiraki, and M. Miyao, J. Appl. Phys. **50**, 5966 (1979).
[6] J. R. Haynes and H. B. Briggs, Phys. Rev. **86**, 647 (1952).
[7] J. R. Haynes and W. C. Wesphal, Phys. Rev. **101**, 1676 (1956).
[8] D. Shaughnessy, B. Li, A. Mandelis, and J. Batista, Appl. Phys. Lett. **84**, 5219 (2004).
[9] J. Batista, A. Mandelis, D. Shaughnessy, and B. Li, J. Phys. (Paris) (submitted).
[10] A. Mandelis, J. Appl. Phys. **97**, 083508 (2005).
[11] A. Mandelis, *Diffusion-Wave Fields: Mathematical Methods and Green Functions* (Springer, New York, 2001), Chap. 9.
[12] S. M. Sze, *Physics of Semiconductor Devices*, 2nd ed. (Wiley, New York, 1981), Chap. 7.2.
[13] D. E. Kane and R. W. Swanson, J. Appl. Phys. **72**, 5294 (1992).
[14] J. F. Young and H. M. van Driel, Phys. Rev. B **26**, 2147 (1982).
[15] W. M. Bullis and H. R. Huff, J. Electrochem. Soc. **143**, 1399 (1996).
[16] A. G. Aberle, S. Glunz, and W. Warta, J. Appl. Phys. **71**, 4422 (1992).
[17] L. Jastrzebski, O. Milic, M. Dexter, J. Lagowski, D. DeBusk, K. Nauka, R. Witowski, M. Gordon, and E. Persson, J. Electrochem. Soc. **140**, 1152 (1993).
[18] K. L. Luke and L. J. Cheng, J. Appl. Phys. **61**, 2282 (1987); D. K. Schroder, IEEE Trans. Electron Devices **44**, 160 (1997).
[19] E. O. Johnson, Phys. Rev. **111**, 153 (1958).
[20] A. G. Aberle, J. Schmidt, and R. Brendel, J. Appl. Phys. **79**, 1491 (1996).
[21] J. Schmidt and A. G. Aberle, J. Appl. Phys. **81**, 6186 (1997).
[22] M. Schoefthaler, R. Brendel, G. Langguth, and J. H. Werner, *Proceedings of the First WCPEC, Hawaii*, 5–9 December 1994 (unpublished), p. 1509.
[23] C.-M. Li, T. Sjodin, and H.-L. Dai, Phys. Rev. B **56**, 15252 (1997).
[24] T. Ikari, A. Salnick, and A. Mandelis, J. Appl. Phys. **85**, 7392 (1999).
[25] ASTM Standard F723-88, *1996 Annual Book of ASTM Standards* (American Society of Testing Materials, West Conshohocken, PA, 1996).